Mon. Not. R. Astron. Soc. **000**, 1–13 () Printed 1 December 2005 (MN LATEX style file v2.2)

Saturation properties of the Archontis dynamo.

Robert Cameron[1⋆] and David Galloway [2]†
[1] *Max-Planck-Institut für Sonnensystemforschung, Max-Planck-Straße 2, D-37191 Katlenburg-Lindau, Germany*
[2] *School of Mathematics and Statistics, University of Sydney, NSW 2006, Australia*

ABSTRACT
This paper discusses the generation and subsequent non-linear limiting of magnetic fields by motions in a periodic flow driven by a force whose components are proportional to $(\sin z, \sin x, \sin y)$. This problem was originally studied by Archontis (2000); the purpose of the present work is to remove certain complications present in the original model in order better to understand the underlying physical mechanism which limits the total magnetic energy growth. At high Reynolds numbers the resulting dynamos end up with almost equal total magnetic and kinetic energies, and thus yield fields strong enough to be astrophysically relevant. Until now the existence of such dynamos has been doubted, so this demonstration of an example appears very important. At least up to Reynolds numbers of 800, these solutions are laminar and attracting.

We then present an argument showing that any stationary, incompressible dynamo can be used to create a family of solutions with an arbitrary ratio of magnetic to kinetic energies in the limit of large Reynolds numbers. The stability of such solutions is also discussed.

Key words: MHD; magnetic fields.

1 INTRODUCTION

Magnetic fields in many astrophysical objects are thought to arise due to dynamo action associated with motions in electrically conducting fluids. This possibility was first suggested by Larmor (1919), and the subsequent development of dynamo theory can be seen in several textbooks, for example Roberts (1967), Moffatt (1978), Krause & Rädler (1980) and Rüdiger & Hollerbach (2004).

Most recently, two questions as to the astrophysical significance of dynamo action have been considered. The first concerns kinematic dynamos, where the Lorentz force is too weak to react back on the motion responsible for the dynamo. The issue is whether the growth of the magnetic field is fast or slow: whether the timescale for growth of magnetic field is the electromagnetic diffusion time or the turnover time of the flow. The former is unacceptably long in most cases of astrophysical interest, at least if laminar diffusivities are used. A number of fast dynamos have now been exhibited numerically, and a key theoretical result has been established: flows must be chaotic to be capable of fast dynamo action. This result was formally proved by Klapper & Young (1995). In practice most flows in astrophysics are turbulent, so this condition is likely to be satisfied, and at least the kinematic stages of any dynamo will be satisfactory. Fast dynamo theory is fully described in the book of Childress & Gilbert (1995), and is also reviewed in Galloway (2003).

The second question is whether a fast dynamo can attain final field strengths with enough magnetic energy to explain what is actually observed. Recent work on mean field dynamos has cast considerable doubt on this, and an active debate is still in progress (Vainshtein & Cattaneo 1992; Gruzinov & Diamond 1994; Blackman 2002; Diamond et al. 2005). Most of the work has been done in the context of mean field electrodynamics, for which the difficulties are summarised by the terms "catastrophic α or β-quenching". In the non-scale-separated case, similar problems are also encountered in examples such as the forced ABC dynamos (Galanti et al. 1992; Brummell et al. 2001). These dynamos all have filamentary magnetic field structures, and scaling arguments can be given which suggest that the ratio of total magnetic to kinetic energies tends to zero as the (kinetic) Reynolds number tends to infinity (Brummell et al. 2001; Galloway 2003). Note Moffatt & Proctor (1985) have argued that filamentary structure is an essential prerequisite for fast dynamo action, so on the face of it this is bad news.

In this paper we refrain from commenting on mean field dynamos, but instead concentrate on a class of flows where it is possible to exhibit strong-field dynamos where the total magnetic and kinetic energies are comparable, and, in the limit where Reynolds numbers tend to infinity, equal. These dynamos were first introduced by Archontis (2000);

⋆ E-mail: cameron@linmpi.mpg.de
† E-mail: dave@maths.usyd.edu.au

here we present more extensive calculations which use an incompressible rather than a compressible equation of state, and we try with partial success to understand the underlying physics in terms of the flow geometry. In particular we show that the fields generated are *not* filamentary, but are nonetheless sustained by filamentary features embedded at key places in the flow geometry. This gives a demonstration that strong field dynamos can actually exist, albeit in a flow with a very specific and artificial forcing. Amazingly, the final state of the calculation is steady, though depending on the initial conditions the evolution to this state can take many diffusion times. Thus the equilibration of the dynamo is slow even though its kinematic growth phase is fast. This type of dynamo appears to be possible over a range of ratios of viscous to ohmic diffusivities, stretching at least over values between 0.25 and 4.

Whilst Archontis's flow gives the first clear demonstration that this kind of strong field dynamo is possible, it should be noted models for the generation of the Earth's magnetic field routinely yield total magnetic energies well in excess of the total kinetic energy (Glatzmaier & Roberts 1995), though the kinetic and magnetic Reynolds numbers are far lower than in the astrophysical case (Li et al. 2002). Also Cattaneo (1999) has computed three-dimensional solutions showing magnetoconvective dynamo action in a Boussinesq layer, and finds a total magnetic energy of around 20% of the total kinetic energy, for kinetic and magnetic Reynolds number of around 200 and 1000 respectively. So strong field dynamos are not unprecedented.

Section 2 sets the scene by describing the formulation of the problem in terms of the specified forcing and the governing equations; everything takes place in a 2π-periodic geometry, so that no scale-separation effects are taken into account. Section 3 gives detailed descriptions of the results and an interpretation of what they mean. This section includes a truncated expansion model which reproduces some of the Fourier mode amplitudes. Section 4 briefly sketches the way in which we think the structures found in section 3 are linked to produce this dynamo. A more general theory demonstrating the existence of such dynamos and discussing their stability is presented in section 5. This is followed by a conclusion which assesses the significance of these results in the general context of astrophysical dynamo theory.

2 FORMULATION OF THE PROBLEM

The incompressible forced dynamo problem can be written in the non-dimensional form

$$\frac{\partial \mathbf{B}}{\partial t} = (\mathbf{B}\cdot\nabla)\mathbf{U} - (\mathbf{U}\cdot\nabla)\mathbf{B} + \eta\nabla^2\mathbf{B} \quad (1)$$

$$\frac{\partial \mathbf{U}}{\partial t} = -(\mathbf{U}\cdot\nabla)\mathbf{U} + (\mathbf{B}\cdot\nabla)\mathbf{B} + \nu\nabla^2\mathbf{U} + \mathbf{F} - \nabla\mathbf{P} \quad (2)$$

$$\nabla\cdot\mathbf{U} = 0 \quad (3)$$

$$\nabla\cdot\mathbf{B} = 0 \quad (4)$$

Here $\mathbf{U}$ and $\mathbf{B}$ are the velocity and magnetic fields, η and ν are dimensionless diffusivities, $\mathbf{F}$ is the applied driving force, and P is sum of the gas pressure and kinetic energy density. The forcing $\mathbf{F}$ is free to be specified, and in this paper we usually take it to be equal to $\nu(\sin z, \sin x, \sin y)$. This is similar to the choice made in Archontis (2000); see also Dorch & Archontis (2004) and Archontis et al. (2005). We assume all other quantities are similarly 2π-periodic in space; thus the possibility of scale-separation is not treated in this paper. Archontis chose this particular forcing because of the result in Galloway & Proctor (1992) that the *flow* $\mathbf{U} = (\sin z, \sin x, \sin y)$, hereafter called the sines flow, seems to be a good candidate for a kinematic fast dynamo. However, it should be noted that the sines flow does not arise from a sines forcing because it has non-zero $\mathbf{U}\times(\nabla\times\mathbf{U})$ term; unlike the *ABC* flows where the idea of forcing was first used (Galloway & Frisch 1987), the sines flow is not Beltrami and to force it successfully when there is no magnetic field present one must also include an extra contribution which balances this term. If this is actually done, the sines flow does indeed arise, but only at low Reynolds numbers, up to approximately $1/\nu = 8$. Above this value, the sines flow is unstable, and becomes time-dependent and turbulent. Very surprisingly though, the introduction of a small magnetic field restores the motion to something close to the sines flow, providing one waits long enough.

Whilst ν and η can be thought of in some sense as inverse kinetic and magnetic Reynolds numbers, it is ν, η and the force which are specified in advance, with the velocity and hence the actual values of the Reynolds numbers being determined by the evolution of the system. Where they explicitly appear in what follows, the Reynolds numbers Re and Rm refer to their actual values calculated using the evolved flow.

The force $\mathbf{F}$ that we use in this paper is actually a minor variation of the one used by Archontis (2000). He had a time dependent scalar which allowed the amplitude of the forcing to change. He adjusted this amplitude to maintain an approximately constant kinetic energy. Additionally he considered a fully compressible plasma, with an energy equation and equation of state to obtain the pressure. For simplicity and mathematical clarity, we instead specified a constant-amplitude forcing and an incompressible fluid. Despite these differences both systems evolve to laminar time-independent states, with compressibility playing essentially no role.

When $\nu = \eta = 0$, all solenoidal fields which have $\mathbf{U} = \pm\mathbf{B}$ are solutions to the momentum and induction equations. They are called Elsässer solutions, and are neutrally stable (Friedlander & Vishik 1995). On the other hand, Abarbanel & Holm (1987) argue that non-magnetic 3-D Euler flows are likely to be unstable. Hence the instability of the non-magnetic sines flow may have little bearing on the stability of the magnetic system. Ideal instability results are notoriously ineffective in providing insight into what happens when small diffusivities are added, but it seems at least a possibility that an appreciable subset of $\mathbf{U} = \mathbf{B}$[1] systems could be stable attractors.

The numerical method used to solve the governing equations is straightforward and standard. All variables were expanded in complex Fourier series and time-stepped using

[1] There is a minor complication in that whilst $\mathbf{U}$ is a vector $\mathbf{B}$ is a pseudovector, changing sign when we switch the handedness of the coordinate system. We therefore assume throughout this paper that we are using a right-handed coordinate system. Since the MHD equations have a symmetry $\mathbf{B}\to-\mathbf{B}$, so that for every dynamo solution with $\mathbf{B}=\mathbf{B_0}$ there is another with $\mathbf{B}=-\mathbf{B_0}$, this restriction simplifies the notation without affecting the physics.

a semi-exact Adams-Bashforth scheme with pseudospectral treatment of nonlinear terms, as described in Peyret (2002), pp. 208-210. Our code conserves $\nabla \cdot \mathbf{B} = 0$, and $\nabla \cdot \mathbf{U} = 0$, which were monitored to ensure that they did not grow due to roundoff error.

The code was tested in the linear regime against some of the well studied growth rates for the ABC fast dynamo, and in the non-linear regime against the results of Galanti et al. (1992), who used a virtually identical numerical method. We also confirmed the results of Archontis (2000), who used finite-difference methods and included compressibility.

3 RESULTS

The following results are all for the case where the forcing is proportional to the viscosity, so that $\mathbf{F} = \nu(\sin z, \sin x, \sin y)$. It could be argued that when ohmic losses are an important dissipation mechanism, there should be an extra contribution proportional to η, however since most of our simulations and discussion were for the case where the magnetic Prandtl number $\mathrm{p_m} = \nu/\eta$ was equal to 1, we used this form of the forcing. We return to this issue briefly in section 3.4 where we discuss the effect of varying $\mathrm{p_m}$. Until then we shall assume $\eta = \nu$. In all cases the system eventually evolves into a state with $\mathbf{U} \approx \mathbf{B}$. In the zero-diffusivity limit this becomes exact, and $\mathbf{U}$ and $\mathbf{B}$ both become equal to something which is almost $0.5(\sin z, \sin x, \sin y)$ but which differs from it by a quantity which remains finite as $\nu \to 0$. Remarkably, this solution is steady for all the Reynolds numbers we have considered.

We first give results where for computational economy we begin with an initial condition $\mathbf{U} = \mathbf{B} = \mathbf{F}/\nu$; in this case the system evolves to the above-mentioned steady state, taking a few diffusion times to get there. This process is shown in Fig. 1 for $1/\eta = 1/\nu = 100$, which gives plots of the evolution of total kinetic and magnetic energies. To study scaling behaviour we use this type of intitial condition with different values of $\eta = \nu$; later we examine the important question of how the steady state is reached if instead we start with a small seed magnetic field, so that there is a kinematic phase followed by a subsequent dynamical equilibration. This requires a substantially longer calculation. Finally, we show cases with varying magnetic Prandtl number to see whether it makes any difference which diffusivity mechanism is dominant.

First we take the standard forcing as described above, and perform computations with $1/\eta = 1/\nu = 50, 100, 200, 400$ and 800. Our calculations were run with 16, 32, 64, 96 or 128 cubed Fourier modes. After the calculations had approached their equilibria at a given fairly low resolution, a process which often took up to many thousands of dimensionless time units, the resolution was incrementally increased, up to 96 or 128 cubed. At each stage the code was run for several more diffusive timescales. This procedure allowed us to reach low values of ν and η at a reasonable computational cost. For all the cases we ran, the energy levels evolved to time-independent levels (see Fig. 1 for an example). The time independence was also checked for various Fourier modes. We call these steady state solutions of (1)–(4) with this forcing, which lie near $\mathbf{B} = \mathbf{U} = \frac{1}{2}(\sin z, \sin x, \sin y)$, the Archontis family of dynamos. We

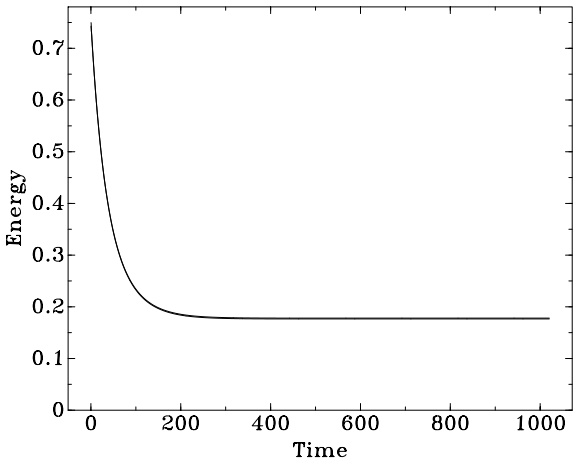

Figure 1. Evolution of kinetic and magnetic energies as a function of time for the Archontis flow with $1/\eta = 1/\nu = 100$, beginning with the initial condition $\mathbf{U} = \mathbf{B} = (\sin z, \sin x, \sin y)$. On this scale the difference between the kinetic and magnetic energies cannot be seen.

again stress that the asymptotic limit as $\eta = \nu \to 0$ is close to but distinct from this, as we shall soon see.

In Fig. 2 we plot the equilibrium magnetic and kinetic energies as a function of $1/\eta = 1/\nu$. It can be seen that they approach the same level as $1/\nu$ becomes large. The way in which this happens can be seen in the difference between the equilibrium values of KE and ME as a function of $1/\nu$ (Fig. 3). This last figure shows that the difference between the energies decays, apparently like $\nu^{1.68}$; if this behaviour persists for larger values of $1/\nu$, then asymptotically $\mathbf{U} = \mathbf{B}$. In any case case the difference between the kinetic and magnetic energies can be written as

$$KE - ME = \int_{\mathrm{volume}} \frac{1}{2}(U^2 - B^2) dV$$

$$KE - ME = \frac{1}{2} \int_{\mathrm{volume}} (\mathbf{U} - \mathbf{B}) \cdot (\mathbf{U} + \mathbf{B}) dV$$

Since $\mathbf{U}+\mathbf{B}$ is large, and tends to some constant vector, it is plausible that the variation in the energies comes from $\mathbf{U} - \mathbf{B}$. This motivates us to use Elsässer variables $\mathbf{\Lambda}_- = \mathbf{U} - \mathbf{B}$ and $\mathbf{\Lambda}_+ = \mathbf{U} + \mathbf{B}$.

The spatial structures of $\mathbf{\Lambda}_+$ and $\mathbf{\Lambda}_-$ are partly revealed in Fig 4 where we show isosurfaces of $|\mathbf{\Lambda}_+|$ for $1/\eta = 1/\nu = 200$ and in Figs 5 and 6 where isosurfaces of $|\mathbf{\Lambda}_-|$ are shown for $1/\eta = 1/\nu = 200$ and 400. Because at high R_m $\mathbf{U}$ and $\mathbf{B}$ are close (but not equal!) to $\frac{1}{2}(\sin z, \sin x, \sin y)$, and $\mathbf{\Lambda}_+$ to $(\sin z, \sin x, \sin y)$, isosurfaces of these quantities are smooth and relatively uninformative. The same applies to several other derived quantities: the current and vorticity are close to $\frac{1}{2}(\cos y, \cos z, \cos x)$; the kinetic and magnetic energies and the cross-helicity $\mathbf{U} \cdot \mathbf{B}$), are all close to $\frac{1}{4}(\sin^2 z + \sin^2 x + \sin^2 y)$; and fluid and current helicities are close to $\sin z \cos y + \sin x \cos z + \sin y \cos x$. For this reason most of our images will be of $\mathbf{\Lambda}_-$, which is more revealing.

We can gain additional insight into $\mathbf{\Lambda}_-$ and $\mathbf{\Lambda}_+$ by looking at some of the Fourier modes (see Figs 7–10). The slowest decaying modes of $\mathbf{\Lambda}_+$ appear to tend to non-zero

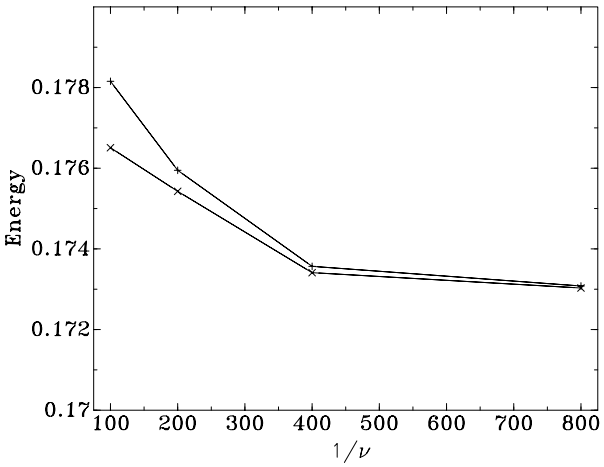

Figure 2. The equilibrium values of the magnetic and kinetic energies are shown as a function of $1/\eta = 1/\nu$.

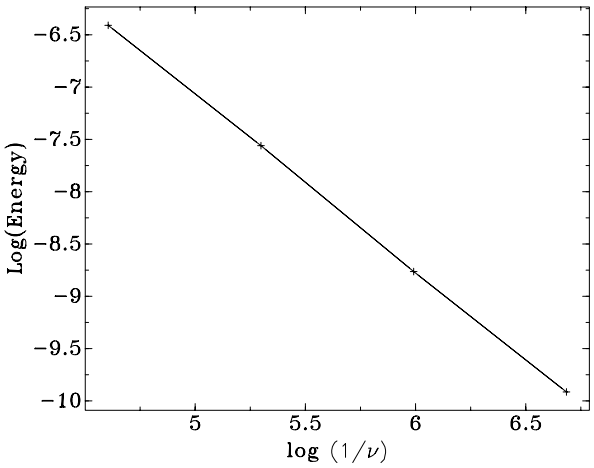

Figure 3. As for figure 2 except the plot is of the log of the difference between the kinetic and magnetic energies, and the x-axis is the log of $1/\nu$. The slope of this line is -1.68.

constant values for large $1/\eta = 1/\nu$, whilst the modes of $\mathbf{\Lambda}_-$ decay at rates between ν and 1.707ν for small $\eta = \nu$. Eventually the modes which decay faster then ν will become much smaller than the modes which decay like ν, so that asymptotically the largest modes in $\mathbf{\Lambda}_-$ will decay like ν. This motivates us to look at the evolution equations for $\mathbf{\Lambda}_-$ and $\mathbf{\Lambda}_+$, which are

$$\frac{\partial \mathbf{\Lambda}_-}{\partial t} = -(\mathbf{\Lambda}_+ \cdot \nabla)\mathbf{\Lambda}_- + \nu\nabla^2\mathbf{\Lambda}_- + F - \nabla P \quad (5)$$

$$\frac{\partial \mathbf{\Lambda}_+}{\partial t} = -(\mathbf{\Lambda}_- \cdot \nabla)\mathbf{\Lambda}_+ + \nu\nabla^2\mathbf{\Lambda}_+ + F - \nabla P \quad (6)$$

$$(7)$$

and

$$\nabla \cdot \mathbf{\Lambda}_- = 0 \quad (8)$$

$$\nabla \cdot \mathbf{\Lambda}_+ = 0 \quad (9)$$

These equations have an obvious symmetry, where $\mathbf{\Lambda}_+$ and $\mathbf{\Lambda}_-$ are swapped. This symmetry corresponds to the fact that the direction of $\mathbf{B}$ can be reversed in equations (1) to (4). Hereafter we only discuss solutions where $\mathbf{\Lambda}_-$ is close to zero.

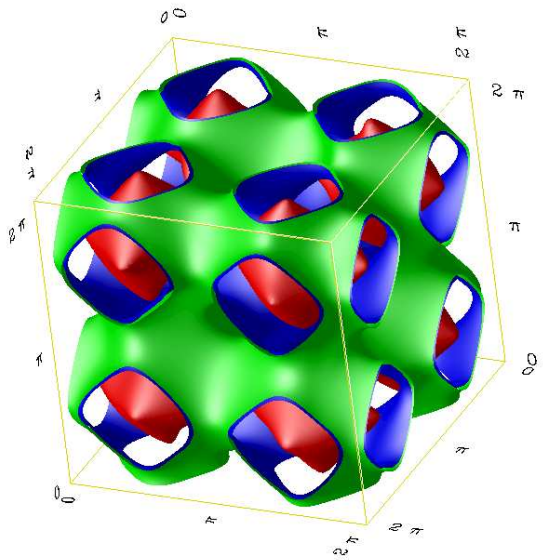

Figure 4. The Archontis solution for $1/\eta = 1/\nu = 200$. The red isosurface is where $(\mathbf{U}+\mathbf{B})\cdot(\mathbf{U}+\mathbf{B})$ exceeds 80% of its maximum value, the green/blue surface shows where it exceeds 50% (with the blue side indicating higher levels). The structure has most of its energy in the $(\sin z, \sin x, \sin y)$ mode. The resulting image is thus smooth.

3.1 Behaviour throughout the bulk of the flow

The above equations are non-linear and very difficult to treat analytically. The numerical solutions give us some insight into the structure of the solutions which we can exploit. For example we have seen that at small ν, $\mathbf{\Lambda}_+$ tends to some non-zero field whereas $\mathbf{\Lambda}_-$ decays like ν. We can therefore look for an approximate solution by dropping terms which are of order ν^2. By further restricting our attention to time independent solutions, we obtain

$$-(\mathbf{\Lambda}_+ \cdot \nabla)\mathbf{\Lambda}_- + \nabla P = -\mathbf{F} \quad (10)$$

$$-(\mathbf{\Lambda}_- \cdot \nabla)\mathbf{\Lambda}_+ + \nabla P = -\mathbf{F} - \nu\nabla^2\mathbf{\Lambda}_+ \quad (11)$$

$$\nabla \cdot \mathbf{\Lambda}_- = 0 \quad (12)$$

$$\nabla \cdot \mathbf{\Lambda}_+ = 0 \quad (13)$$

These equations apply except in limited regions near the 1-D heteroclinic orbits joining different stagnation points, where $\nabla^2\mathbf{\Lambda}_-$ does not go to 0 as ν tends to 0 (see section 3.2).

We want to find a spatially periodic solution to equations (10) to (12). The problem is still nonlinear and difficult. We can further exploit our numerical results by noting that both $\mathbf{\Lambda}_+$ and $\mathbf{\Lambda}_-$ have the symmetry $\mathbf{\Lambda}_\pm(x,y,z)\cdot\hat{\mathbf{x}} = \mathbf{\Lambda}_\pm(y,z,x)\cdot\hat{\mathbf{y}} = \mathbf{\Lambda}_\pm(z,x,y)\cdot\hat{\mathbf{z}}$. Even this is not enough to make the system tractable, and we have sought a truncated solution.

For this we use the fact that in the numerical solution for $\mathbf{\Lambda}_+$ there is more than an order of magnitude between the amplitudes of the most energetic mode $(\sin z, \sin x, \sin y)$, and the second most energetic one. This can be exploited by taking $\mathbf{\Lambda}_{+_0} = (\sin z, \sin x, \sin y)$ as a zeroth order approximation. We use this only on the left hand side of equations (10) to (12) where $\mathbf{\Lambda}_{+_0}$ contributes to many Fourier modes through the non-linear terms. This is not true on the right hand side where $\mathbf{\Lambda}_{+_0}$ contributes to only one mode

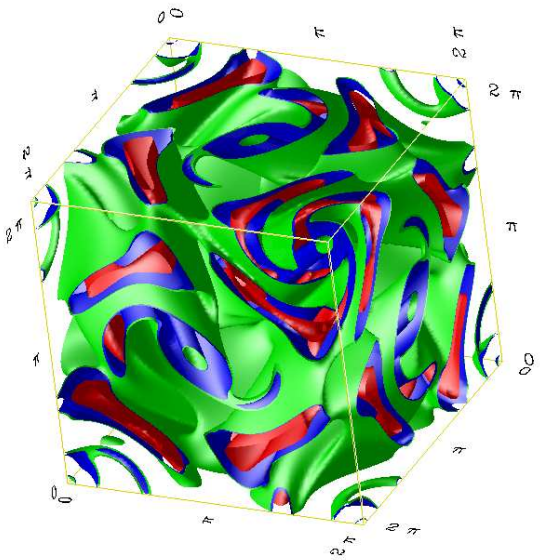

Figure 5. Isosurfaces of $(\mathbf{U}-\mathbf{B})\cdot(\mathbf{U}-\mathbf{B})$ The red isosurface is where it exceeds 80% of its maximum value, the green/blue surface where it exceeds 50%. The cores of the "cigars" are thin, straight tubes. The cross-section of one of these tubes is visible as a small green circle at the vertex $(2\pi, 2\pi, 2\pi)$, in the centre of the image. Others are at the midpoints of the visible sides of the cube.

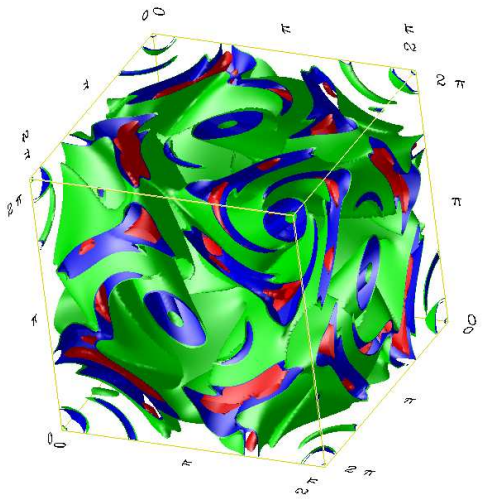

Figure 6. As for figure 5 except for $1/\eta = 1/\nu = 400$. Little has changed, except the region of weak field surrounding the heteroclinic orbits has shrunk.

of $-\nu\nabla^2\mathbf{\Lambda}_+$. Fortunately we can (in principle) solve equation (10) for $\mathbf{\Lambda}_-$ using the approximate value $\mathbf{\Lambda}_{+0}$ and then use equation 12 to find a better estimate of $\mathbf{\Lambda}_+$.

The problem then becomes

$$-((\sin z,\sin x,\sin y)\cdot\nabla)\mathbf{\Lambda}_- + \nabla P = -\mathbf{F} \quad (14)$$

$$-(\mathbf{\Lambda}_-\cdot\nabla)(\sin z,\sin x,\sin y) + \nabla P = -\mathbf{F} - \nu\nabla^2\mathbf{\Lambda}_+ \quad (15)$$

$$\nabla\cdot\mathbf{\Lambda}_- = 0 \quad (16)$$

$$\nabla\cdot\mathbf{\Lambda}_+ = 0 \quad (17)$$

This linear set of PDEs approximates the full non-

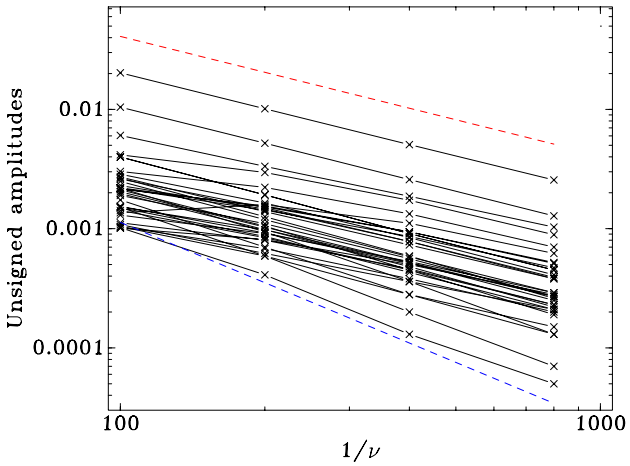

Figure 7. Unsigned amplitudes of the Fourier modes of $\mathbf{\Lambda}_-$ whose unsigned amplitude exceeds $5\times10^{-3}/800$. at $1/\eta = 1/\nu = 100$, 200, 400 and 800 are shown. The dashed red curve shows a decay rate ν^1 and the blue curve a decay rate of $\nu^{1.68}$. All these modes are decaying, at a rate that appears to be a constant power of ν. Many of the modes appear to decay like ν for large $1/\nu$.

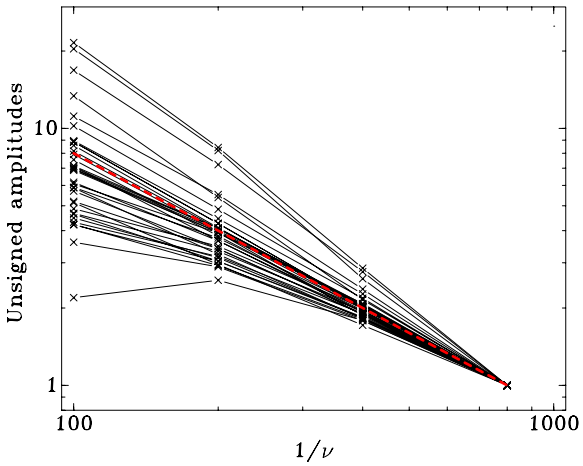

Figure 8. Similar to Fig. 7 we here show the unsigned amplitudes of the Fourier modes of $\mathbf{\Lambda}_-$. The main difference is that all the curves are now normalised by their values at $1/\nu = 800$. Only those modes whose unsigned amplitude exceeds 0.01/800. at $1/\eta = 1/\nu$=100, 200, 400 and 800 are shown. Many of the even modes appear to decay like ν (indicated by the dashed red line) for large $1/\nu$, with one or two decaying more quickly.

linear system. It is still too difficult for us to solve. We therefore considered a Fourier series expansion of $\mathbf{\Lambda}_-$ and $\mathbf{\Lambda}_+$ (implicitly assuming the solution is periodic). Using the software package Maxima, we included all modes with $|l|+|m|+|n| < 9$ (where l, m, and n are wavenumbers in the three directions). To close the resulting system we assumed the coefficients of $\cos 6x \sin y \cos z$, $\cos 5x \cos y \sin 2z$, and $\sin 5x \sin 2y \sin z$ were zero. These closure conditions were taken from the numerical simulation, but possibly reflect underlying symmetries.

The modes with largest amplitude, either in the numerical calculation or in the approximate solution, are given in Tables 1 and 2. The match appears to be reasonable, especially for the largest few modes. To find the amplitudes of the remaining modes requires a better estimate of $\mathbf{\Lambda}_+$

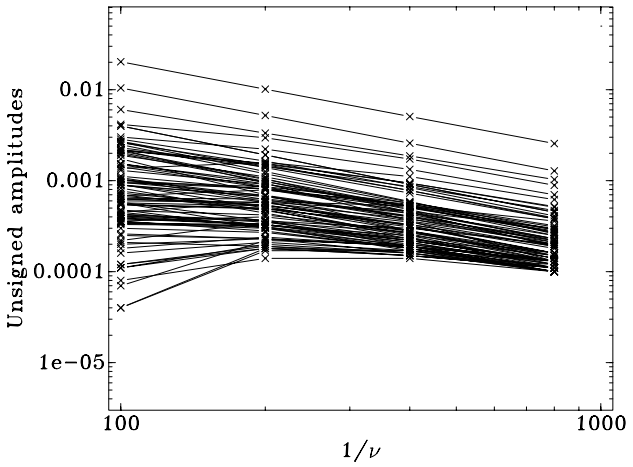

Figure 9. Again, as for Fig. 7 except here we look at all modes with an unsigned amplitude at $1/\nu = 800$ greater than 10^{-4} at $1/\eta = 1/\nu = 100$, 200, 400 or 800. The selection criteria used in Fig. 7 is possibly biased to detect decaying modes. The current selection criteria is not biased. At low amplitudes the picture is messy, but no modes which grow with $1/\nu$ appear to be present (the presence of any such mode would indicate that the solutions weren't asymptotically valid).

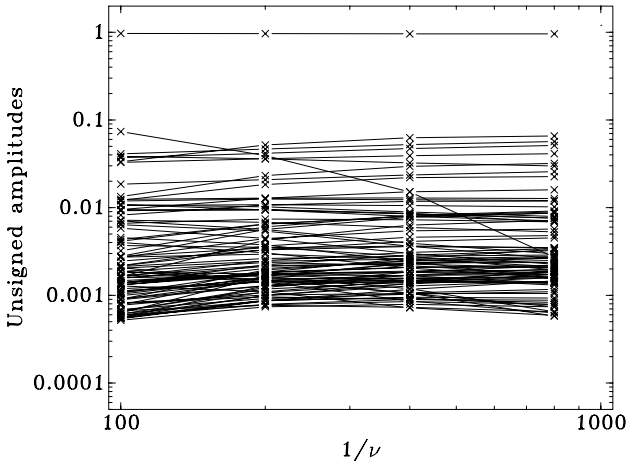

Figure 10. Unsigned amplitudes of the Fourier modes of $\mathbf{\Lambda}_+$. Only those modes whose unsigned amplitude exceeds 10^{-3} at $1/\eta = 1/\nu =$100, 200, 400 and 800 are shown. Most of the values of $\mathbf{\Lambda}_+$ appear to be tend towards constant values as $1/\eta = 1/\nu$ increases. A few are decaying. The uppermost curve with an energy near 1 is the $(\sin z, \sin x, \sin y)$ mode.

than$\mathbf{\Lambda_{+0}}$. The newly found approximation for $\mathbf{\Lambda}_+$ would presumably lead to a better match, and the procedure outlined here could be applied iteratively, although whether this would constitute an improvement on a full time-dependent solution is debatable.

3.2 Behaviour near the straight heteroclinic orbits

We now consider those regions where $\nabla^2\mathbf{\Lambda}_-$ does not fall to 0 as $\nu \to 0$ and for which the above analysis does not apply. These regions have been found numerically to be regions immediately surrounding the 1-D heteroclinic orbits. Heteroclinic orbits are important topological features, especially in the theory of 3-D reconnection (Priest & Forbes 2000),

x-component of $\mathbf{\Lambda}_-$

mode	Simulation	Analysis
$\sin y \cos z$	-2.05 Rm^{-1}	$-2\mathrm{Rm}^{-1}$
$\sin x \sin 2y \sin z$	1.02 Rm^{-1}	$0.95\mathrm{Rm}^{-1}$
$\cos x \cos y \sin 2z$	0.82 Rm^{-1}	$0.63\mathrm{Rm}^{-1}$
$\cos x \sin 2y$	0.50 Rm^{-1}	
$\sin 2x \cos 2z$	-0.36 Rm^{-1}	$-0.34\mathrm{Rm}^{-1}$
$\sin 2x \cos 2y$	0.36 Rm^{-1}	$0.34\mathrm{Rm}^{-1}$
$\cos 2x \sin z$	0.25 Rm^{-1}	
$\cos 2y \sin z$	0.21 Rm^{-1}	
$\cos 2x \sin y \cos z$	0.10 Rm^{-1}	$0.16\mathrm{Rm}^{-1}$
$\sin z$	0.10 Rm^{-1}	

Table 1. Some of the low wavenumber Fourier modes with the high amplitudes at $1/\eta = 1/\nu = 800$. The analysis in the third column is discussed in the text.

x-component of $\mathbf{\Lambda}_+$

mode	Simulation	Analysis
$\sin z$	0.958	1.0
$\sin x \sin 2y \sin z$	-0.066	
$\cos x \sin 2y \cos 2z$	-0.057	-0.056
$\cos x \sin 2y$	-0.051	-0.036
$\sin 2x \sin y \sin 2z$	-0.041	-0.036
$\cos 2x \sin y \cos z$	-0.032	
$\cos 2y \sin z$	0.030	0.034
$\cos 2x \sin z$	0.024	0.018

Table 2. Some of the low order Fourier modes with the highest amplitudes at $1/\eta = 1/\nu = 800$, second column uses simulated. The difference between the numerical calculation and the Maxima result is largely due to the differences in $\mathbf{\Lambda}_-$ in Table 1.

being streamlines (or field lines) which connect stagnation (or magnetic null) points. In the current case of dynamo action, it is the behaviour of $\mathbf{\Lambda}_-$ near the heteroclinic orbits of $\mathbf{\Lambda}_+$ which is important.

Figure 11 shows the geometry of some of the heteroclinic orbits of $\mathbf{U} + \mathbf{B}$ associated with the stagnation point at (π, π, π) for the case $1/\eta = 1/\nu = 400$. Fig. 12 shows the geometry of the plane we are about to discuss; which is perpendicular to the linear heteroclinic orbit passing through it. To show the structure of $\mathbf{\Lambda}_-$ on this plane we introduce $\mathbf{\Lambda}_{-\,\mathrm{normal}}$, the component of the velocity aligned with the heteroclinic orbit, and $\mathbf{\Lambda}_{-\,\mathrm{plane}}$ the projection of $\mathbf{\Lambda}_-$ onto the plane. The colour-scale in Fig. 12 corresponds to $\mathbf{\Lambda}_{-\,\mathrm{normal}}$, whilst the arrows give $\mathbf{\Lambda}_{-\,\mathrm{plane}}$.

A critical feature of this image is the fact that the arrows form tight circles around the heteroclinic orbits. This can be seen better in Fig. 13 where the magnitude of the arrows in from Fig. 12 are plotted. We immediately see that the magnitude of $\mathbf{\Lambda}_{-\,\mathrm{plane}}$ increases until we are only a small distance away from the heteroclinic orbit and then falls quickly to zero at this orbit itself.

3.2.1 Axisymmetric components

Since the situation very near the heteroclinic orbits is largely axisymmetric we have performed an azimuthal averaging to find the behaviour of $\mathbf{\Lambda}_{-\,\mathrm{plane}}$ as a function of the distance from that orbit. The crosses in Fig. 14 show the result. Also

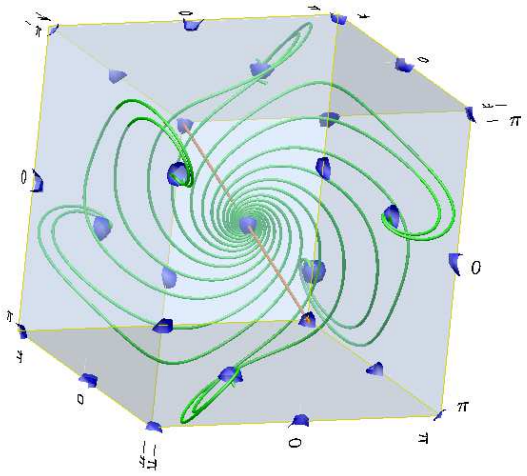

Figure 11. Interesting topological features of $\mathbf{U}+\mathbf{B}$ for the Archontis flow with $1/\eta = 1/\nu = 400$. Shown in blue are the regions near the minima of the kinetic energy. These regions contain stagnation points, which are similar to those of the Sines flow.The green curves lie on the stable manifold of the central stagnation point. The orange curves are heteroclinic orbits on the unstable manifold of the central stagnation point.

shown are the results for $1/\eta = 1/\nu = 200$ (squares) and $1/\eta = 1/\nu = 800$ ("+"s). Figure 15 shows the same results, except we have multiplied the results for $1/\eta = 1/\nu = 800$ by 2 and divided the results for $1/\eta = 1/\nu = 200$ by 2. We see that the three curves overlap except very near the heteroclinic orbit, indicating that away from the latter $\mathbf{\Lambda}_{-\,\mathrm{plane}}$ scales like ν.

In Fig. 16 we have multiplied the results for $1/\eta = 1/\nu = 800$ by $\sqrt{2}$ and divided the results for $1/\eta = 1/\nu = 200$ by $\sqrt{2}$. The curves should now be identical where $\mathbf{\Lambda}_{-\,\mathrm{plane}}$ scales like $\nu^{1/2}$. We can see that this scaling holds in a thin boundary layer of radius $\nu^{1/2}$, surrounding the heteroclinic orbits.

Since Rm scales like ν^{-1} for these flows, our results indicate a scaling for $\mathbf{\Lambda}_-$ of $\mathrm{Rm}^{-1/2}$ in a region of radius $\mathrm{Rm}^{-1/2}$ around the heteroclinic orbit. This implies that $|\mathbf{\Lambda}_-|$, $\frac{|\mathbf{\Lambda}_-|}{r}$, and $|\frac{\partial \mathbf{\Lambda}_{-\,\mathrm{plane}}}{\partial r}|$ converge uniformly to 0 as $\nu \to 0$. In contrast

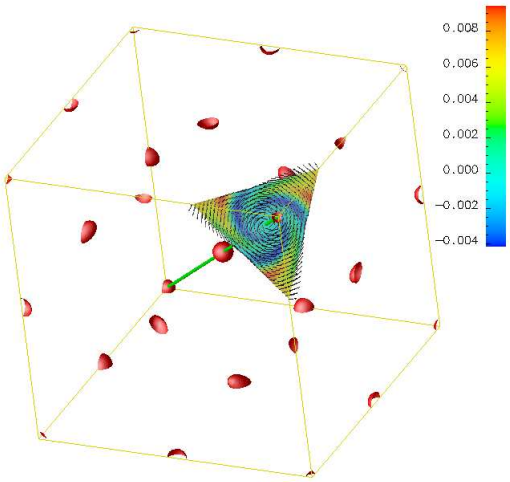

Figure 12. Here we show the plane chosen for subsequent analysis in Figs 13 to 16. On the plane we show the three components of the vector field $\mathbf{\Lambda}_-$. The arrows correspond to the components in the plane, the colouring to the component parallel to the heteroclinic orbit. Near the heteroclinic orbit the arrows almost form circles.

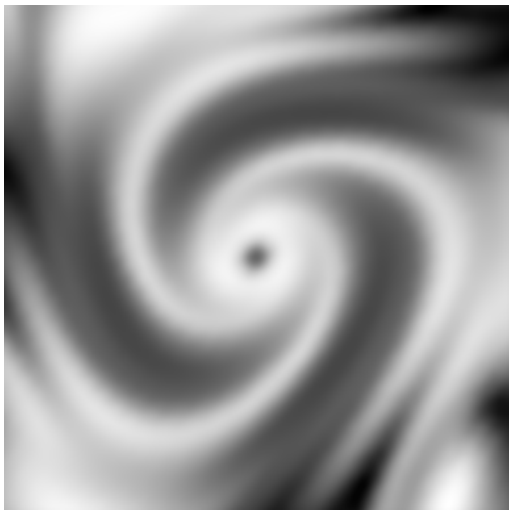

Figure 13. For the plane shown in Fig. 12 (extended using periodicity), we show the magnitude of the components of $\mathbf{\Lambda}_-$ in the plane.

$|\frac{\partial^2 \mathbf{\Lambda}_{-\,\mathrm{plane}}}{\partial r^2}|$ and $|\frac{\mathbf{\Lambda}_{-\,\mathrm{plane}}}{r^2}|$ tend to constant, non-zero values along the heteroclinic orbits. In this $\mathrm{Rm}^{-1/2}$ neighbourhood, the diffusive term in equation (5) cannot be ignored.

3.2.2 Non-axisymmetric components

Also noticeable in Fig. 13 are the spiral arms which merge to form the axisymmetric structure near the heteroclinic orbit. There are six of these spiral arms (three low intensity, three high) which relates to the six-fold symmetry of the 2-dimensional manifolds of the stagnation points: the central stagnation point is connected by pairs of heteroclinic orbits to the stagnation point in the centre of each face of the cube. The relationship between the heteroclinic orbits and

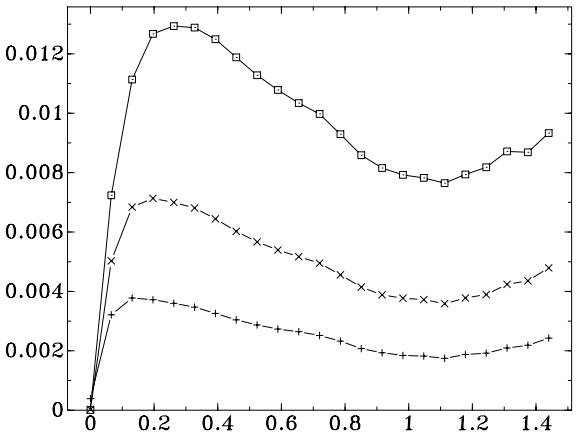

Figure 14. A plot of $|\mathbf{\Lambda}_{-\,\mathrm{plane}}|$ azimuthally averaged, with the x-axis giving the distance from the heteroclinic orbit. The strength falls to zero very rapidly near the heteroclinic orbit. The rapidness of the fall is explored in the next three figures. Squares are used for $1/\eta = 1/\nu = 200$, crosses for $1/\eta = 1/\nu = 400$ and "+"s for $1/\eta = 1/\nu = 800$. There are two different scalings with ν in this graph, as is better shown in the next two plots.

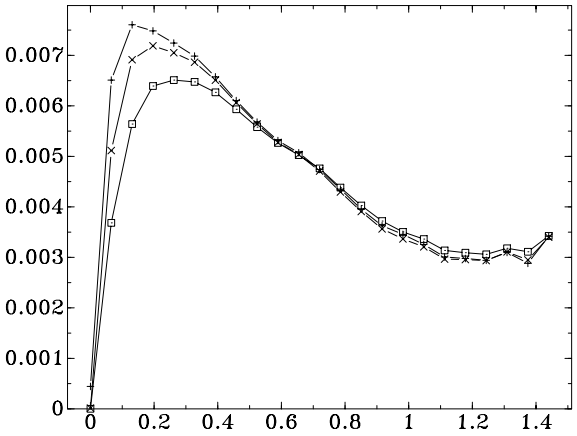

Figure 15. For $1/\eta = 1/\nu = 400$ this plot is identical to Fig. 14. For $1/\eta = 1/\nu = 200$ we have divided the averages by 2, for $1/\eta = 1/\nu = 800$ we have multiplied them by 2. In this way we see that $|\mathbf{\Lambda}_{-\,\mathrm{plane}}|$ scales like ν away from the heteroclinic orbit.

$\mathbf{\Lambda}_{-\,\mathrm{plane}}$ can be better seen in Fig. 17. In this case, where we are looking directly at the unstable manifold, the six-fold symmetry is complete in that there are 6 bright and six dark spiral arms.

The structure of the 2-D stable manifold is itself interesting, particularly since there appear to be exactly two heteroclinic orbits connecting the middle stagnation point with those at the centre of each face. Figure 18 is an attempt to convey the geometry of the 2-D manifold. The main features are consequences of the existence of the pairs of heteroclinic orbits. These structures are almost certainly important for the dynamo action, but why there are precisely two such orbits is an interesting question.

Figure 16. For $1/\eta = 1/\nu = 400$ this plot is identical to Fig. 14. For $1/\eta = 1/\nu = 200$ we have divided the averages by $\sqrt{2}$, for $1/\eta = 1/\nu = 800$ we have multiplied them by $\sqrt{2}$. It is possible to see that $|\mathbf{\Lambda}_{-\,\mathrm{plane}}|$ scales like $\nu^{1/2}$ near the heteroclinic orbit.

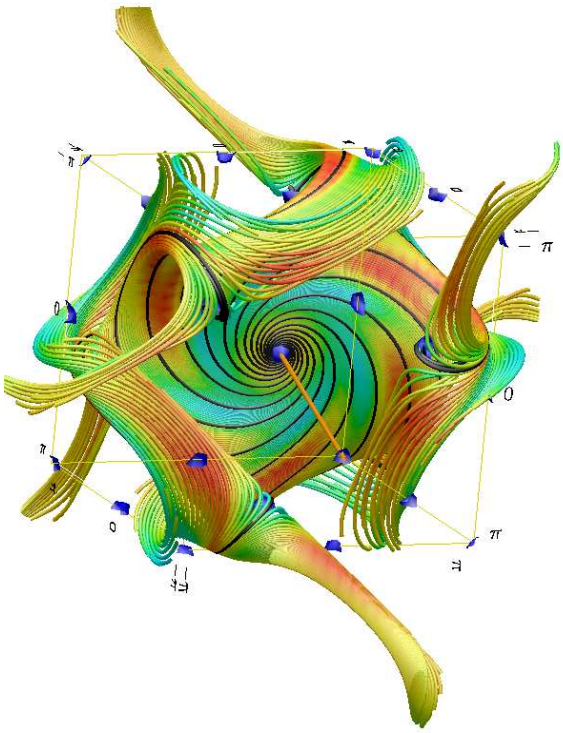

Figure 17. The structure of the 2-D manifold, colour coded by $\mathbf{\Lambda}_{-\,\mathrm{plane}}$. The relationship between the spiral arms and the heteroclinic orbits is apparent.

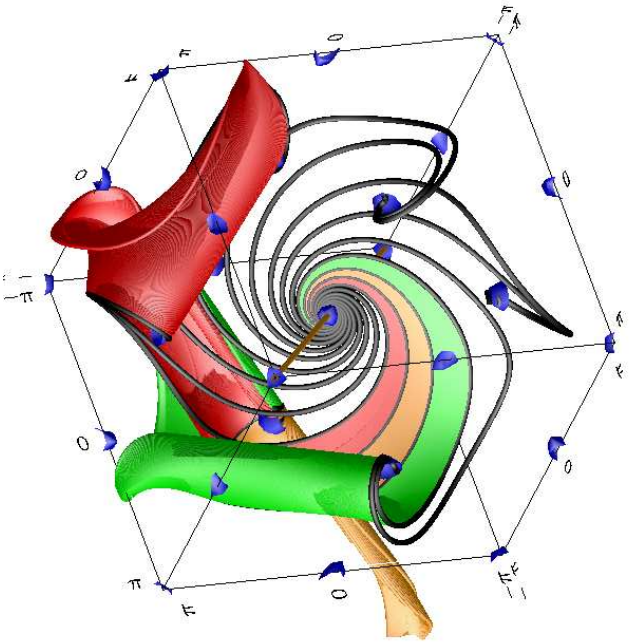

Figure 18. The structure of the 2-D manifold. Three segments of the manifold, separated by heteroclinic orbits, have been coloured. Near the middle stagnation point the orange segment separates the green and the red. However as we approach the stagnation point in the centre of the top face, the orange segment is pulled away from the viewer and the green and red segments meet. The meeting of course takes place along a straight 1-D heteroclinic orbit which is not visible. It is easy to believe this type of structure can efficiently 'stretch, twist and fold' the field.

3.2.3 Coupling the large scale structure to the heteroclinic orbits

As we have seen, very close to the heteroclinic orbits $\mathbf{\Lambda}_-$ has a ϕ component which decays like $1/\mathrm{Rm}$ and falls to zero inside a diffusive boundary layer of thickness $\mathrm{Rm}^{-1/2}$. Slightly further away things become more complicated. Figure 13 shows 6 bright or dark arms which reflect the set of heteroclinic orbits associated with this dynamo.

A full treatment of the whole problem must relate the structure of $\mathbf{U}$ and $\mathbf{B}$ near the heteroclinic orbits to the large scale Fourier modes discussed above via a matched asymptotic expansion. This is very difficult (witness Childress & Soward (1985), who attempted to perform this task for the kinematic ABC dynamo problem), and so far we have made little progress. Our aim here has been to show the type of properties any solution must have if it is to be asymptotic, and to highlight some of the important features associated with dynamo action.

3.3 The Archontis forcing with weak field initial conditions

The previous subsection dealt with the incompressible dynamo equations subject to the Archontis forcing $\mathbf{F}$, with an initial condition $\mathbf{U} = \mathbf{B} = \mathbf{F}/\nu$. We saw that the system evolved towards the Archontis flow. The same state is eventually reached if we begin from a weak seed magnetic field with randomly generated Fourier amplitudes, and take $\mathbf{U} = (\sin z, \sin x, \sin y)$. In this case it takes a long time for the system to evolve to its equilibrium state, and the solution spends many diffusive timescales in an apparently turbulent state, as is shown in Fig. 19 for the case with $\eta = \nu = 100$. Between $t = 100$ and $t = 1200$ both the kinetic and magnetic energies show only small fluctuations which appear to have no systematic structure. The cross-helicity, normalised by the product of the rms speed ($|\mathbf{U}|$) and rms field strength ($|\mathbf{B}|$), shows a systematic increase until its maximum value of nearly one is reached. The cross-helicity normalized in this way is a measure of the alignment between the flow and the field, with a value of one indicating perfect alignment. Figure 19 thus indicates the the flow is almost continuously becoming more aligned as the system evolves. The helicity reaches its equilibrium value around $t = 1250$, and at this stage the magnetic and velocity fields are almost perfectly aligned, and have most of their energy in the $(\sin z, \sin x, \sin y)$ mode. It takes approximately 400 more time units for the the kinetic and magnetic energies to reach their final values.

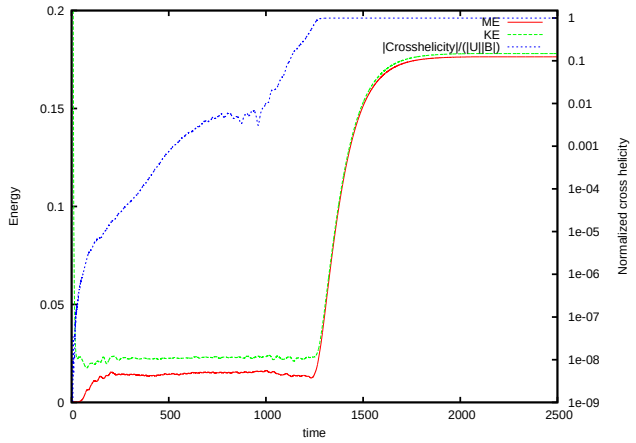

Figure 19. Evolution of kinetic and magnetic energies, as well as the cross helicity, as a function of time. The cross-helicity is shown using the logarithmic scale of the right hand side of the graph whereas the energies use the linear scale on the left. The cross helicity is normalised by $\sqrt{(KE)(ME)}/(8\pi^3)$; the simulation was started with a weak seed magnetic field.

3.4 Behaviour with $\eta \neq \nu$

So far we have restricted our attention to the case where $\eta = \nu$. Now we describe two additional runs, one with $\eta = 1/400$, $\nu = 1/100$ and one with $\eta = 1/100$, $\nu = 1/400$. In both cases we set $\mathbf{F} = \nu(\sin z, \sin x, \sin y)$, and began from the initial condition $\mathbf{U} = \mathbf{B} = \mathbf{F}/\nu$. The time evolution of the sum of, and difference between, the kinetic and magnetic energies is shown in figure 20. When $\eta = 1/400$ and $\nu = 1/100$ the system evolves to a steady state, with Λ_+, U_0 and B_0 similar to what is found when $\eta = \nu$ ($= 1/400$ or $1/100$, except with less energy. This change is presumably because the driving force which provides the energy scales scales like ν whereas the ohmic losses scale like η.

The case with $\eta = 100$ and $\nu = 400$ evolved to a state

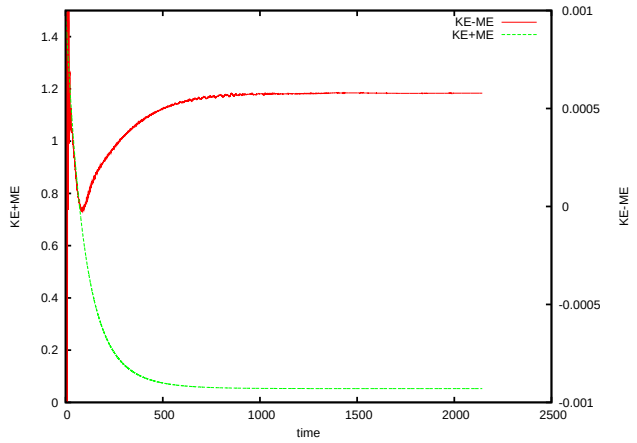

Figure 20. Evolution of the sum of (green), and difference between (red), the kinetic magnetic energies as a function of time for the case $\nu = 1/400$ and $\eta = 1/100$. Note the sum uses the scale on the left hand side of the graph, whereas the difference use that on the right.

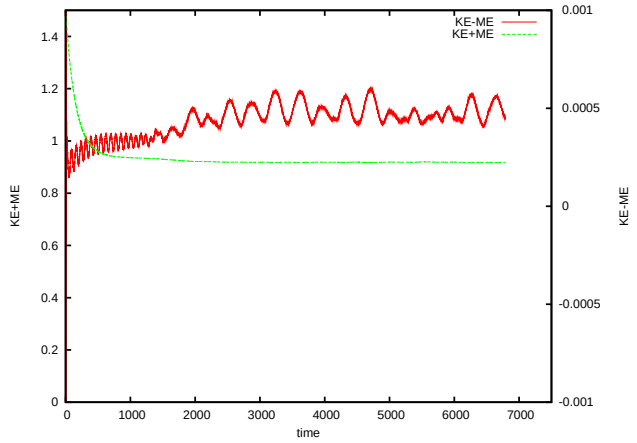

Figure 21. This figure is similar to Fig.20, except it shows the evolution when $\nu = 1/100$ and $\eta = 1/400$.

which was not quite time-independent, with very small irregular oscillations superimposed on a static background field. The oscillations are similar in magnitude to $\mathbf{\Lambda}_-$. The evolution is shown in Fig. 21; the energy level is considerably higher than in the cases where $\nu = \eta$, which relates to the way we have scaled $\mathbf{F} = \nu(\sin z, \sin x, \sin y)$. We have not investigated whether scaling the force with $\frac{\nu+\eta}{2}$ would make the system time independent.

4 FAST DYNAMO ACTION

The actual sines-flow itself is apparently a fast dynamo (Galloway & Proctor 1992; Galloway & O'Brian 1993). The Archontis flow is not exactly the sines flow, but has similar features. In particular we have shown that its heteroclinic orbits (Fig. 11) are associated with important boundary layer structures of thickness $\mathrm{Rm}^{-1/2}$. This is the same region where the cigar shaped eigenmodes of the fast sines-flow dynamo form. In order to investigate the relevance of fast dynamo action, we performed a kinematic experiment using the velocity field from the equilibrium associated with an Archontis dynamo having $\eta = \nu = 1/800$. Using this velocity field, we found the eigenmodes of the kinematic dynamo problem with $\eta = 100$ grew rapidly, with eigenfunctions similar to those of the sines flow.

Returning to the fully non-linear Archontis dynamo, we suspect that the essential dynamo action is occurring near the heteroclinic orbits. It is in this region that unsigned flux is being generated. However the flux does not remain in the cigars but diffuses into the bulk of the plasma. The equilibrium velocity field associated with $\eta = \nu = 1/800$ needs to transport less flux than the velocity associated with the case $\eta = \nu = 1/100$, since the flux in the bulk of the volume decays much more rapidly in the latter case. Using the velocity field associated with $\eta = \nu = 1/800$ in a kinematic calculation with $\eta = \nu = 1/100$ therefore leads to the observed accumulation of flux in the vicinity of the heteroclinic cigars. In the Archontis dynamo this flux is transported by advection and diffusion into the bulk of the flow.

We can proceed slightly further by estimating the rate at which such a mechanism can produce unsigned flux. The kinematic cigars have a characteristic radius $\mathrm{Rm}^{-1/2}$ and hence a characteristic cross-sectional area Rm^{-1}. They grow on the turnover timescale, which implies that the field grows like $e^{\sigma t}$, where σ is some positive constant independent of Rm. The total unsigned flux through any plane grows as $\mathrm{Rm}^{-1}e^{\sigma t}$, the factor of Rm^{-1} appearing because it is the area occupied by the strong field. Assuming that the field strength in the vicinity of the of the heteroclinic orbit is $O(1)$ then the rate of flux generation scales like Rm^{-1}. In the kinematic sines flow, this flux remains concentrated in an $\mathrm{O}(\mathrm{Rm}^{-1/2})$ sheath around the heteroclinic orbit, and the dynamo action is fast.

The magnetic field in the bulk of the plasma undergoes ohmic decay, which destroys flux at a rate $\mathrm{Rm}^{-1}|B|$ where $|B|$ is the typical field strength. Since the rate of flux generation and decay both scale like Rm^{-1} we have the possibility of generating an O(1) field in the bulk of the fluid.

The basic physical picture we have in mind is similar to the kinematic, rotor dynamos of Herzenberg (1958). The essential idea of these is that the flow occurs only in small rotating spheres which are embedded in a stationary medium. Given a seed field each rotor creates an induced field which then diffuses out to the other rotors. This transported field acts as their seed field, and they in turn provide the seed field for the original rotor, closing the loop. The Archontis dynamo apparently operates in a similar way, with the heteroclinic orbits playing the role of the rotors and the transport being via both advection and diffusion. A conceptual sketch of this is shown in Fig. 22: the corresponding sketch for the rotor dynamo would be similar except the flux would be entirely diffusive.

The kinematic examples of Herzenberg (1958), Gibson (1968a), Gibson (1968b), Gailitis (1970) and others are powerful tools for understanding $\mathbf{U} \sim \mathbf{B}$ dynamos, a point we will return to in a future paper (Cameron & Galloway, submitted).

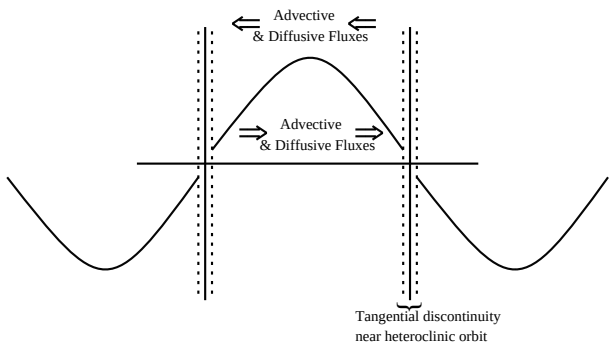

Figure 22. A sketch to indicate how we believe the large scale field is generated and maintained by dynamo action localised near the heteroclinic orbits. In reality the dynamo is fully three-dimensional. The idea is similar to that underlying the rotor dynamo of Herzenberg. The velocity in the rotor dynamos is restricted to the rotation of small cylinders embedded in a non-moving fluid. Given a seed magnetic field each rotor generates magnetic flux which is transported by diffusion to the other rotors where it fulfills the role of the seed field. We suggest that the physical picture is similar for the Archontis dynamo with the heteroclinic orbits playing the role of the rotors and the transport between the heteroclinic orbis occurring via advection and diffusion rather than via diffusion alone.

5 EXISTENCE AND STABILITY OF FAMILIES OF U ∼ B DYNAMOS

5.1 Existence

Suppose that we have some stationary solution ($\mathbf{U_0}$, $\mathbf{B_0}$) of the induction equation with $\eta = \eta_0$, obtained either with dynamics included or as a marginal solution to the kinematic problem. This just means that $\mathbf{U_0}$ and $\mathbf{B_0}$ are solutions to equations (1), (3) and (4), and the associated boundary conditions. Then, since the induction equation is linear in $\mathbf{B}$, ($\mathbf{U_0}$, $\alpha\mathbf{B_0}$) is also a solution. Exploiting a different symmetry, we also have ($\epsilon\mathbf{U_0}$, $\alpha\mathbf{B_0}$) is a solution for $\eta = \epsilon\eta_0$: effectively all the terms in the induction equation have just been multiplied by ϵ which does not affect the equality. Furthermore, because the component of $\mathbf{U}$ in the direction of $\mathbf{B}$ plays no role in the induction equation, $\mathbf{U} = \beta\mathbf{B_0} + \epsilon\mathbf{U_0}$ and $\mathbf{B} = \alpha\mathbf{B_0}$ is also a solution when $\eta = \epsilon\eta_0$. This solution is valid for all α, β and ϵ.

The crucial point is that we can now include the dynamics. For each solution to equations (1), (3) and (4) discussed above, we can regard the momentum equation as defining that $\mathbf{F}$ which produces a stationary solution. This can be done for any value of $\mathrm{p_m}$, with the result that

$$\begin{aligned}\mathbf{F} &= +\epsilon^2(\mathbf{U_0}\cdot\nabla)\mathbf{U_0} \\ &\quad +\beta\epsilon(\mathbf{U_0}\cdot\nabla)\mathbf{B_0} \\ &\quad +\beta\epsilon(\mathbf{B_0}\cdot\nabla)\mathbf{U_0} \\ &\quad +(\beta^2-\alpha^2)(\mathbf{B_0}\cdot\nabla)\mathbf{B_0} \\ &\quad -\nu_0\epsilon^2\nabla^2\mathbf{U_0} - \nu_0\epsilon\beta\nabla^2\mathbf{B_0}. \end{aligned} \quad (18)$$

The induction equation implies

$$\eta_0\nabla^2\mathbf{B_0} = -(\mathbf{B_0}\cdot\nabla)\mathbf{U_0} + (\mathbf{U_0}\cdot\nabla)\mathbf{B_0} \quad (19)$$

so that

$$\begin{aligned}\mathbf{F} &= +\epsilon^2(\mathbf{U_0}\cdot\nabla)\mathbf{U_0} \\ &\quad -\nu_0\epsilon^2\nabla^2\mathbf{U_0} \\ &\quad +(\beta^2-\alpha^2)(\mathbf{B_0}\cdot\nabla)\mathbf{B_0} \\ &\quad +\beta\epsilon(\mathbf{U_0}\cdot\nabla)\mathbf{B_0} \\ &\quad +\beta\epsilon(\mathbf{B_0}\cdot\nabla)\mathbf{U_0} \\ &\quad -\mathrm{p_{m_0}}\epsilon\beta\left(-(\mathbf{B_0}\cdot\nabla)\mathbf{U_0} + (\mathbf{U_0}\cdot\nabla)\mathbf{B_0}\right). \end{aligned} \quad (20)$$

This solution can be scaled to give arbitrary ratios of the total magnetic to kinetic energy, at arbitrary values of the diffusivities. The solution asymptotically approaches $\mathbf{U} = \beta\mathbf{B_0}$ and $\mathbf{B} = \alpha\mathbf{B_0}$ as $\epsilon \to 0$. Furthermore, when $\alpha = \beta = 1$ and $\mathrm{p_m} = 1$, the force is

$$\begin{aligned}\mathbf{F} &= +\epsilon^2(\mathbf{U_0}\cdot\nabla)\mathbf{U_0} \\ &\quad -\epsilon^2\nu_0\nabla^2\mathbf{U_0} \\ &\quad +2\epsilon(\mathbf{B_0}\cdot\nabla)\mathbf{U_0} \end{aligned} \quad (21)$$

This result is exact, however its relationship to the Archontis dynamo is only approximate. The force used to drive the Archontis flow is $\mathbf{F} = \nu(\sin z, \sin x \sin y)$ which scales with ϵ as $\nu = \epsilon\nu_0$ is varied; the second order terms in the equation 21 do not appear in the Archontis forcing. These terms, scaling with ϵ^2, will be small, and are likely to have a role only near the heteroclinic orbits where terms of this order dominate. Even with this limitation, this theory gives us a framework in which some of the properties of the Archontis dynamo solution can be understood. It also leads back to the analysis in section 3 – to leading order, equation (21) is

$$\mathbf{F} = 2\epsilon(\mathbf{B_0}\cdot\nabla)\mathbf{U_0} + \nabla P. \quad (22)$$

This is very similar to equation (10), when we substitute $\mathbf{\Lambda}_+ \approx 2\mathbf{B_0}$ and $\mathbf{\Lambda}_- = \epsilon\mathbf{U_0}$.

5.2 Stability

The existence of such solutions is of no astrophysical significance unless they are stable. The numerical solutions also suggest an approach for tackling the stability problem. From an initial condition near the steady state, $\mathbf{\Lambda}_+ = \mathbf{U} + \mathbf{B}$ the evolution is only slow (on the diffusive timescale) whereas $\mathbf{\Lambda}_-$ initially has large oscillations which are quickly damped and thereafter also only evolves on the slow timescale, see Fig.23. The central idea of the following analysis is the decoupling of the fast and slow behaviours.

We restrict our attention to the case $\alpha = \beta = 1$ so that the equilibrium values of $\mathbf{\Lambda}_+$ and $\mathbf{\Lambda}_-$ are $\mathbf{\Lambda_{+eq}} = 2\mathbf{B_0}+\epsilon\mathbf{U_0}$ and $\mathbf{\Lambda_{-eq}} = \epsilon\mathbf{U_0}$, respectively. We linearise Equations (5)–(9) by writing $\mathbf{\Lambda}_+ = \mathbf{\Lambda_{+eq}} + \boldsymbol{\lambda}_+$ and $\mathbf{\Lambda}_- = \mathbf{\Lambda_{-eq}} + \boldsymbol{\lambda}_-$ and ignoring terms which are second order in $\boldsymbol{\lambda}_{+/-}$. Equations (5)–(9) then become

$$\begin{aligned}\epsilon\frac{\partial\boldsymbol{\lambda}_-}{\partial t} &= \epsilon\left(-(\mathbf{\Lambda_{+eq}}\cdot\nabla)\boldsymbol{\lambda}_- - (\boldsymbol{\lambda}_+\cdot\nabla)\mathbf{\Lambda_{-eq}} + \epsilon\eta_0\nabla^2\boldsymbol{\lambda}_-\right) \\ &\quad -\nabla\psi \end{aligned} \quad (23)$$

$$\begin{aligned}\frac{\partial\boldsymbol{\lambda}_+}{\partial t} &= \epsilon\left(-(\mathbf{\Lambda_{-eq}}\cdot\nabla)\boldsymbol{\lambda}_+ - (\boldsymbol{\lambda}_-\cdot\nabla)\mathbf{\Lambda_{+eq}} + \eta_0\nabla^2\boldsymbol{\lambda}_+\right) \\ &\quad -\nabla\psi \end{aligned} \quad (24)$$

$$\nabla\cdot\boldsymbol{\lambda}_- = 0 \quad (25)$$

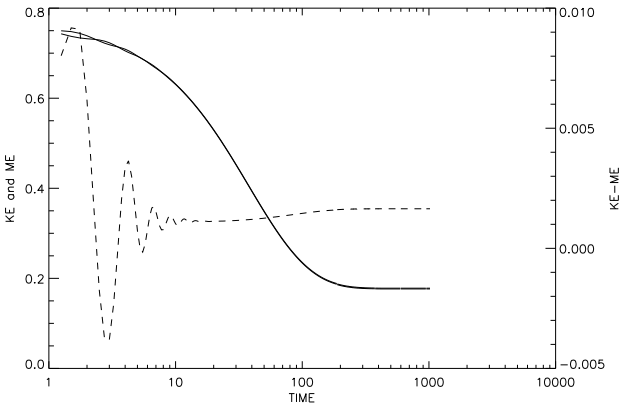

Figure 23. The kinetic and magnetic energies (solid curves, using the left axis) as a function of time. The difference between the energies is shown using the dashed curve and the right axis. This plot is for the case $1/\eta = 1/\nu = 100$ started from $\mathbf{U} = \mathbf{B} = (\sin z, \sin x, \sin y)$.

$$\nabla \cdot \boldsymbol{\lambda}_+ = 0 \tag{26}$$

Here ψ, the pressure perturbation, is determined by the requirement that equations (25) and (26) are satisfied. It follows from this that ψ will be of the same order as the other terms in equation (24), that is it will scale like ϵ.

This formulation of the problem is consistent with the idea that the expected evolution of $\boldsymbol{\lambda}_+$ will be slow. The evolution of $\boldsymbol{\lambda}_-$ is more complicated. On the fast turnover time of the flow $\boldsymbol{\lambda}_+$ will be almost fixed and therefore $(\boldsymbol{\lambda}_+ \cdot \nabla)\boldsymbol{\Lambda}_-$ will be effectively constant in equation (23). This term can be balanced by $(\boldsymbol{\Lambda}_+ \cdot \nabla)\boldsymbol{\lambda}_-$ in a quasi-static fashion, with $\boldsymbol{\lambda}_-$ only evolving with $\boldsymbol{\lambda}_+$ on the slow timescale. This motivates the introduction of $\boldsymbol{\lambda}_{\mathbf{-qs}}$ which obeys

$$-(\boldsymbol{\Lambda}_{\mathbf{+eq}} \cdot \nabla)\boldsymbol{\lambda}_{\mathbf{-qs}} - (\boldsymbol{\lambda}_+ \cdot \nabla)\boldsymbol{\Lambda}_{\mathbf{-eq}} - \nabla\psi_{\rm qs} = 0 \tag{27}$$

where $\nabla\psi_{\rm qs}$ is chosen so that $\nabla \cdot \boldsymbol{\lambda}_{\mathbf{-qs}} = 0$ is satisfied. This allows us to rewrite equation (23):

$$\begin{aligned} \frac{\partial(\boldsymbol{\lambda}_- - \boldsymbol{\lambda}_{\mathbf{-qs}})}{\partial t} &+ (\boldsymbol{\Lambda}_{\mathbf{+eq}} \cdot \nabla)(\boldsymbol{\lambda}_- - \boldsymbol{\lambda}_{\mathbf{-qs}}) \\ &+ \nabla\psi - \epsilon\nu_0\nabla^2(\boldsymbol{\lambda}_- - \boldsymbol{\lambda}_{\mathbf{-qs}}) \\ &= -\frac{\partial \boldsymbol{\lambda}_{\mathbf{-qs}}}{\partial t} + \epsilon\nu_0\nabla^2\boldsymbol{\lambda}_{\mathbf{-qs}} \end{aligned} \tag{28}$$

The left hand side of this equation is linear in $(\boldsymbol{\lambda}_- - \boldsymbol{\lambda}_{\mathbf{-qs}})$ and has constant coefficients. The solutions to the homogeneous equation is of the form of damped (Alfvén) waves. These waves, and a low amplitude equilibrium solution, are driven by the terms on the right hand side. As we have seen the evolution of $\boldsymbol{\lambda}_{\mathbf{+qs}}$ is slow so the magnitude of these terms scales like ϵ. Thus $\boldsymbol{\lambda}_-$ will be driven to its quasi-static value whilst producing only small amplitude oscillations. When ϵ is small these oscillations will not significantly affect the slow evolution of $\boldsymbol{\lambda}_+$, their effect being of $\mathrm{O}(\epsilon^2)$, and we can assume that $\boldsymbol{\lambda}_-$ obeys equation (27). Equation (24) then becomes

$$\begin{aligned} \frac{\partial \boldsymbol{\lambda}_+}{\partial t} &= \epsilon\left(-(\boldsymbol{\Lambda}_{\mathbf{-eq}} \cdot \nabla)\boldsymbol{\lambda}_+ - (\boldsymbol{\lambda}_{\mathbf{-qs}} \cdot \nabla)\boldsymbol{\Lambda}_{\mathbf{+eq}} + \nu_0\nabla^2\boldsymbol{\lambda}_+\right) \\ &\quad -\nabla\psi \end{aligned} \tag{29}$$

Rescaling the evolution of $\boldsymbol{\lambda}_+$ to the slow timescale using $t^* = \epsilon t$ we derive

$$\begin{aligned} \frac{\partial \boldsymbol{\lambda}_+}{\partial t^*} &= -(\boldsymbol{\Lambda}_{\mathbf{-eq}} \cdot \nabla)\boldsymbol{\lambda}_+ - (\boldsymbol{\lambda}_{\mathbf{-qs}} \cdot \nabla)\boldsymbol{\Lambda}_{\mathbf{+eq}} + \nu_0\nabla^2\boldsymbol{\lambda}_+ \\ &\quad -\nabla\psi^* \end{aligned} \tag{30}$$

where ψ^* is again chosen to make $\nabla \cdot \boldsymbol{\lambda}_+$ vanish

Under the above assumptions, the evolution of $\boldsymbol{\lambda}_+$, is independent of ϵ, implying that if the system is stable for some value of ϵ it will be stable for all higher values. However, the argument is not rigorous because we have ignored terms which are second order in ϵ, and as previously discussed these terms are important near the heteroclinic orbits. We have presented this analysis simply because so far it is the closest we have been able to come to an understanding of the stability.

6 DISCUSSION

The Archontis dynamo does not fall exactly within the above theory because its forcing lacks the quadratic term for the family of solutions discussed in the last section. It is for this reason that the structure of $\boldsymbol{\Lambda}_-$ in the vicinity of the heteroclinic orbits is seen to change with $\eta = \nu$. Nonetheless, the Archontis dynamo is closely related, and its features can be partly understood in terms of the theory.

This dynamo is important because it is an example of a laminar dynamo where the nonlinear terms govern the equilibrium field strength. Suprisingly it is also time independent. It defeats the filamentary scalings put forward in Galloway (2003), and shows that there are dynamos which fall outside this class. Laminar dynamos exist which saturate with a magnetic energy comparable to the kinetic energy. This behaviour extends over a range of values of Rm and Re and we found no evidence that it is not asymptotic.

The evolution of this dynamo to its steady state is slow, and seems to depend on diffusion acting throughout the bulk of the domain. This prompts us to consider the question of whether dynamos exist where the build up of the magnetic energy to levels similar to the kinetic energy occurs on the turnover timescale of the flow. Clearly such a dynamo must be fast, otherwise the dynamo would take a diffusive timescale just to leave the kinematic phase. However being fast implies that it is filamentary (Moffatt & Proctor 1985). Since the Lorentz force and the magnetic energy density both scale like $|\mathbf{B}|^2$ in the kinematic regime, it follows that the magnetic energy will be comparable to $\mathrm{O}(\mathrm{Re}^{-1})$ as we leave the kinetic regime (Galloway 2003). However, the kinetic energy, being unaffected by the magnetic field, will be of order 1. To maintain the fast evolution, the magnetic field must then lose its filamentary form and become space filling. The only apparent way for this to occur is for the dynamo to continually restructure itself on the fast timescale as the magnetic field grows. The natural extension of the fast dynamo question is thus: at very high Reynolds numbers can the magnetic field grow to a level comparable with the kinetic energy at a rate which is bounded below by a positive constant? In other words, can laminar flows produce astrophysically relevant field strengths on reasonable timescales? None of the examples we have considered so far have achieved this, but we intend to adress this issue by con-

sidering a range of forcing terms, with various dependencies on ν and η, in the future.

We have shown steady dynamos exist for all ratios of the total magnetic to kinetic energies, even for large Re and Rm. Not all of these dynamos will be stable but we have found some, including the Archontis dynamo, which are. The latter saturates with its total magnetic energy equal to its kinetic energy in the limit of large Reynolds numbers. However, scaling arguments have been given to show *any* ratio of magnetic energy to kinetic energy is possible – one just has to choose the right force.

ACKNOWLEDGEMENTS

DJG is grateful for the opportunity to participate in the Isaac Newton Institute's session "Magnetohydrodynamics of Stellar Interiors" at Cambridge, UK, where this study was completed. We benefited greatly from discussions on this topic with other participants, in particular Axel Brandenburg, Pat Diamond, Andrew Gilbert, Mike Proctor, and Alexander Ruzmaikin, several of whom stressed the importance of the cross-helicity or attempted to make analytic progress. The paper also benefited from useful comments by an anonymous referee.

Some of the calculations were performed at the GWDG (Gesellschaft für wissenschaftliche Datenverarbeitung Göttingen). We made extensive use of the software packages Maxima, OpenDX, ANA and FFTW3, and we thank all those responsible for their existence.

REFERENCES

Abarbanel H., Holm D., 1987, Phys. Fluids, 30, 3369
Archontis V., 2000, PhD thesis, University of Copenhagen
Archontis V., Dorch S. B. F., Nordlund A., 2005, A&A, in preparation
Blackman E., 2002 Springer Lecture Notes in Physics, 2002, Recent developments in magnetic dynamo theory, in turbulence and magnetic fields in astrophysics
Brummell N. H., Cattaneo F., Tobias S. M., 2001, Journal of Fluid Dynamics Research, 28, 237
Cameron R., Galloway D., submitted, MNRAS
Cattaneo F., 1999, ApJ, 515, L39
Childress S., Gilbert A. D., 1995, Stretch, twist, fold: the fast dynamo. Springer-Verlag
Childress S., Soward A. M., 1985, in NATO ASIC Proc. 161: Compendium in Astronomy On the rapid generation of magnetic fields. pp 223–244
Diamond P. H., Hughes D. W., Kim E.-J., 2005, in Soward A. M., Jones C. A., Hughes D. W., Weiss N. O., eds, Fluid dynamics and dynamos in astrophysics and geophysics Vol. 12 of The fluid mechanics of astrophysics and geophysics, Self-consistent mean field electrodynamics in two and three dimensions. CRC Press, pp 145–192
Dorch S. B. F., Archontis V., 2004, solar physics, 224, 171
Friedlander S., Vishik M., 1995, Chaos, 5, 416
Gailitis A., 1970, Magnetohydrodynamics, 6, 14
Galanti B., Sulem P. L., Pouquet A., 1992, Geophys. Astrophys. Fluid Dyn., 5158, 1
Galloway D. J., 2003, in Feriz-Mas A., Núñez M., eds, Advances in Nonlinear Dynamos Taylor & Francis, London
Galloway D. J., Frisch U., 1987, J. Fluid Mech., 180, 557
Galloway D. J., O'Brian N. R., 1993, in Proctor M. R. E., Matthews P. C., Rucklidge A. M., eds, Solar and Planetary Dynamos No. 1 in Publications of the Newton Institute, Numerical calculations of dynamos for abc and related flows. Cambridge University Press, pp 105–113
Galloway D. J., Proctor M. R. E., 1992, Nat, 356, 691
Gibson R. D., 1968a, Q. J. Mech. Appl. Math., 21, 243
Gibson R. D., 1968b, Q. J. Mech. Appl. Math., 21, 257
Glatzmaier G. A., Roberts P. H., 1995, Nat, 377, 203
Gruzinov I., Diamond P. H., 1994, Physical Review Letters, 72, 1651
Herzenberg A., 1958, Phil. Trans. Roy. Soc. A, 249, 507
Klapper I., Young L. S., 1995, Comm. Math. Phys., pp 623–646
Krause F., Rädler K. H., 1980, Mean-field magnetohydrodynamics and dynamo theory. Pergamon Press
Larmor J., 1919, Rep. Brit. Assoc. Adv. Sci., pp 159–160
Li J., Sato T., Kageyama A., 2002, Science, 295, 1887
Moffatt H. K., 1978, Magnetic field generation in electrically conducting fluids. Cambridge University Press
Moffatt H. K., Proctor M. R. E., 1985, J. Fluid Mech., 154, 493
Peyret B., 2002, Spectral Methods for Incompressible Viscous Flow. Vol. 148 of Applied Mathematical Sciences, Springer-Verlag
Priest E., Forbes T., 2000, Magnetic Reconnection: MHD theory and applications. Cambridge University Press
Roberts P. H., 1967, An introduction to Magnetohydrodynamics. American Elsevier, New York
Rüdiger G., Hollerbach R., 2004, The magnetic universe : geophysical and astrophysical dynamo theory. Wiley-VCH
Vainshtein S. I., Cattaneo F., 1992, ApJ, 393, 199